

Bi₁₂Rh₃Cu₂I₅: A 3D Weak Topological Insulator with Monolayer Spacers and Independent Transport Channels

Eduardo Carrillo-Aravena, Kati Finzel, Rajyavardhan Ray, Manuel Richter, Tristan Heider, Iulia Cojocariu, Daniel Baranowski, Vitaliy Feyer, Lukasz Plucinski, Markus Gruschwitz, Christoph Tegenkamp, and Michael Ruck*

Topological insulators (TIs) are semiconductors with protected electronic surface states that allow dissipation-free transport. TIs are envisioned as ideal materials for spintronics and quantum computing. In Bi₁₄Rh₃I₉, the first weak 3D TI, topology presumably arises from stacking of the intermetallic [(Bi₄Rh)₃I]²⁺ layers, which are predicted to be 2D TIs and to possess protected edge-states, separated by topologically trivial [Bi₂I₈]²⁻ octahedra chains. In the new layered salt Bi₁₂Rh₃Cu₂I₅, the same intermetallic layers are separated by planar, i.e., only one atom thick, [Cu₂I₄]²⁻ anions. Density functional theory (DFT)-based calculations show that the compound is a weak 3D TI, characterized by Z₂ = (0; 0001), and that the topological gap is generated by strong spin-orbit coupling ($E_{g,calc.} \sim 10$ meV). According to a bonding analysis, the copper cations prevent strong coupling between the TI layers. The calculated surface spectral function for a finite-slab geometry shows distinct characteristics for the two terminations of the main crystal faces <001>, viz., [(Bi₄Rh)₃I]²⁺ and [Cu₂I₄]²⁻. Photoelectron spectroscopy data confirm the calculated band structure. In situ four-point probe measurements indicate a highly anisotropic bulk semiconductor ($E_{g,exp.} = 28$ meV) with path-independent metallic conductivity restricted to the surface as well as temperature-independent conductivity below 60 K.


1. Introduction

Topological insulators (TIs) form a class of materials whose properties are associated with nongeneric quantum effects. Phenomenologically, TIs are semiconductors in the bulk, but possess metallic surface states of a distinctive quality. These surface states are protected by the topology of the bulk electronic structure.^[1] Their momentum (propagation direction) and their spin are locked orthogonally. This stabilization can only be broken by strong perturbation, e.g., by an energy exceeding the topologically nontrivial bandgap of the bulk. As a result, these surface electrons are protected against backscattering from nonmagnetic impurities,^[2] leading to dissipation-free charge transport and preservation of spin orientation under suitable conditions.^[3] Therefore, TIs are envisioned as promising materials for high-performance spin field-effect transistors^[4] and as quantum bits in quantum computing.^[5] Despite the strong interest

in TIs, the number of TIs experimentally proven as well as useable under “real” conditions is still quite limited.

E. Carrillo-Aravena, K. Finzel, M. Ruck
Faculty of Chemistry and Food Chemistry
Technische Universität Dresden
01062 Dresden, Germany
E-mail: michael.ruck@tu-dresden.de

E. Carrillo-Aravena, M. Ruck
Würzburg–Dresden Cluster of Excellence ct.qmat
c/o Technische Universität Dresden
01062 Dresden, Germany

 The ORCID identification number(s) for the author(s) of this article can be found under <https://doi.org/10.1002/pssb.202100447>.

© 2022 The Authors. physica status solidi (b) basic solid state physics published by Wiley-VCH GmbH. This is an open access article under the terms of the Creative Commons Attribution License, which permits use, distribution and reproduction in any medium, provided the original work is properly cited.

DOI: 10.1002/pssb.202100447

R. Ray, M. Richter
Leibniz IFW Dresden
Helmholtzstr. 20, 01069 Dresden, Germany

R. Ray, M. Richter
Dresden Center for Computational Materials Science (DCMS)
Technische Universität Dresden
01062 Dresden, Germany

T. Heider, I. Cojocariu, D. Baranowski, V. Feyer, L. Plucinski
Peter Grünberg Institute PGI-6
Forschungszentrum Jülich
52425 Jülich, Germany

M. Gruschwitz, C. Tegenkamp
Institute of Physics
Technische Universität Chemnitz
Reichenhainer Str. 70, 09126 Chemnitz, Germany

M. Ruck
Max Planck Institute for Chemical Physics of Solids
Nöthnitzer Str. 40, 01187 Dresden, Germany

One type of topological protection in TIs, the earliest proposed theoretically^[6] and verified experimentally,^[7] is based on strong spin–orbit coupling (SOC). The reason is that SOC causes an inversion between states with opposite parities around the bandgap. When such an inverted semiconductor comes into contact with a material with trivial parity sequence (normal semiconductor, air, vacuum), the states with the same parity combine at the interface to form metallic and spin-polarized surface states that cross the bandgap.^[8] As SOC increases with the atomic number and is particularly strong in *p*-orbitals, bismuth, as the heaviest nonradioactive element, is an excellent choice for the synthesis of TI materials. Intensively studied bismuth-based TIs include Bi₂Te₃,^[9] Bi₂Te₂Se,^[10] Bi₂TeBr,^[11] Bi₂TeI,^[12] and MnBi_{2n}Te_{3n+1}.^[13,14]

All these compounds are categorized as strong 3D TI which are bulk materials characterized by protected surface states on all facets.^[15] Moreover, the mentioned Bi compounds are layered materials consisting of stacked 2D TIs.^[6] In addition, there is the comparatively exclusive compound Bi₁₄Rh₃I₉ (**1**), which is the first material with strong experimental and theoretical indications of a weak 3D TI state, implying a crystalline material with protected surface states on certain, but not all, facets.^[16] This bismuth-rich subiodide has a layered structure, in which intermetallic [(Bi₄Rh)₃I]²⁺ TI layers alternate with topologically trivial [Bi₂I₈]²⁻ spacer layers (**Figure 1**). The spacer layer effectively separates the electronic systems of adjacent intermetallic layers that are presumed^[16a] to be 2D TIs. The weak 3D TI **1** is thus a stack of weakly coupled 2D TIs. The spatial density of TI channels in stacking direction, a quantity that could be of interest for applications, is 0.8 nm⁻¹. The topological bandgap of compound **1** is large (about 240 meV), implying that the TI quantum state exists at room temperature (RT) and above.

Explicit understanding of the relationships between chemical composition and crystal structure on the one hand and topological properties of the electronic band structure on the other hand is important for synthesis of potentially viable TIs. In this regard, compounds similar to **1** have recently been studied. The chemically and structurally closely related layered bismuth platinum subiodides (**Figure 1**), Bi₁₃Pt₃I₇ (**3**),^[17,18] Bi₁₂Pt₃I₅ (**4**),^[18]

Bi₃₈Pt₉I₁₄,^[19] Bi₈Pt₅I₃,^[20] or Bi₁₆Pt₁₁I₆,^[20] unfortunately, are not TIs suitable for electronic applications because of bulk conductivity caused by nonmatching electron count and/or electronic coupling of the predicted 2D TI layers. In particular, a monolayer of iodide ions, as present in **3** or **4**, was found to be an insufficient spacer as covalent Bi–I–Bi bonds strongly couple adjacent intermetallic layers.^[18,21] This is different in the weak 3D TI Bi₁₂Rh₃Cu₂I₅ (**2**) presented here. The goal of this research was to replace the spacer layer in **1** while preserving the predicted 2D TI character of the intermetallic layer, thus obtaining further insights into tuning and designing principles of new layered weak 3D TIs based in both structural (physical) and chemical criteria.

2. Results and Discussion

2.1. Synthesis and Thermal Stability

To explore possible phase formation in the Bi–Rh–Cu–I quaternary system and derive optimal reaction conditions, we performed differential scanning calorimetry (DSC) measurements starting from mixtures of Bi, Rh, Cu, and BiI₃ in 0.1 mL silica ampoules and characterized the products associated with the detected DSC signals. In the course of these studies, we detected the new compound **2**. The DSC experiment of a mixture with the composition of the target compound is shown in **Figure 2**.

The reactions were assigned to their respective signals (**Table 1**) based on phase diagrams^[22,23] and analysis of the products of ex situ annealing experiments (**Figure S4–S8**, Supporting Information). The first endothermic effect at 265 °C (H1) was assigned to the melting of Bi. The liquid phase induces the formation of binary and ternary phases, initially Bi₁₈I₄^[22] and γ-CuI are predominant. The signal H2 was attributed to the decomposition of Bi₁₈I₄, being the only phase not observed anymore in a reaction mixture annealed at 297 °C. The latter also contained the cluster salt (Bi₈)₂(Bi₉)[RhBi₆I₁₂]₃^[24] along with reflections associated with at least one unreported Bi–Cu–I compound, which is currently under investigation. The endothermic effect H3 is

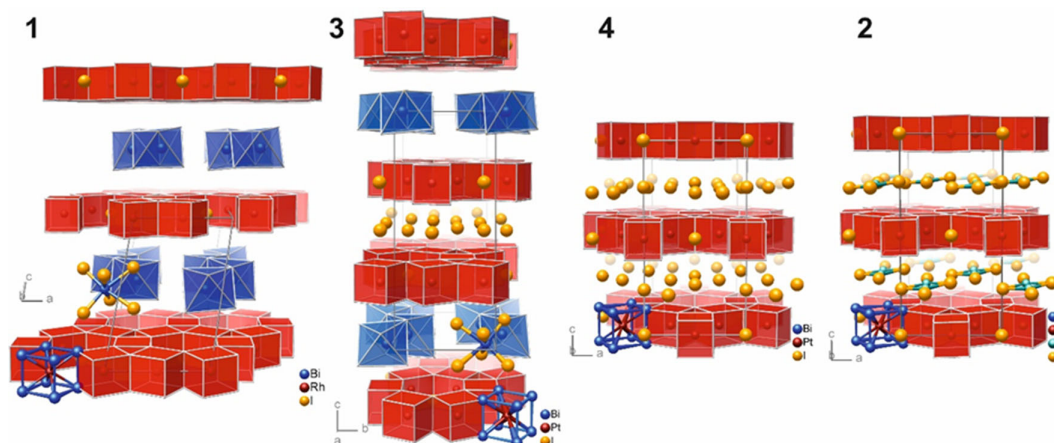


Figure 1. From left to right: crystal structures of the bismuth-rich subiodides Bi₁₄Rh₃I₉ (**1**), Bi₁₃Pt₃I₇ (**3**), Bi₁₂Pt₃I₅ (**4**), and Bi₁₂Rh₃Cu₂I₅ (**2**). In all compounds, the Rh- or Pt-centered Bi cubes form the same kagome nets, which host iodide ions in their hexagonal voids. These predicted 2D TI layers are separated by different spacers: iodidobismuthate(III) chains in **1** and **3**, monolayers of isolated iodide ions in **3** and **4**, or iodidocuprate(I) groups in **2**.

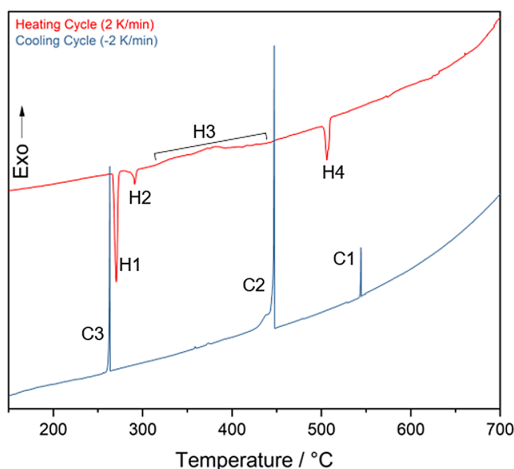


Figure 2. Thermal analysis (DSC) of a mixture of Bi, BiI₃, Rh, and Cu with the molar ratio of 31:5:9:6, which corresponds to the composition of **2**. The heating curve is shown in red and the subsequent cooling curve in blue.

Table 1. Assignment of DSC signals in Figure 2 (H = heating, C = cooling). The listed temperatures for the signals are the onset temperatures, except for the signal H3, which covers a broad range.

Signal	Temperature [°C]	Assigned Process
H1	265	Melting of Bi; beginning of formation of binary and ternary phases
H2	281	Decomposition of Bi ₁₈ I ₄
H3	320–430	Formation of Bi ₁₂ Rh ₃ Cu ₂ I ₅ (peak maximum at about 380 °C)
H4	500	Decomposition of Bi ₁₂ Rh ₃ Cu ₂ I ₅
C1	545	Crystallization of β-Bi ₂ Rh
C2	448	Crystallization of Bi ₁₂ Rh ₃ Cu ₂ I ₅
C3	264	Crystallization of Bi

associated with the formation of **2**. Trace amounts of this compound were already observed at lower temperatures, suggesting that its formation is kinetically hindered. Upon reaching 500 °C (H4), **2** decomposes following the reaction $\text{Bi}_{12}\text{Rh}_3\text{Cu}_2\text{I}_5 \rightarrow 3\text{Bi}_2\text{Rh} + 2\text{CuI} + 5\text{Bi} + \text{BiI}_3$, which was confirmed by further DSC experiments starting from manually selected crystals of **2** (Figure S1 and Table S1, Supporting Information).

Combining this information with the optimized synthesis protocol for compound **1**,^[16b] we developed temperature programs for the targeted synthesis of single-phase microcrystalline powders as well as for growing larger crystals of **2**. The new subiodide **2** forms black plate-shaped crystals with {001} as the largest faces. **2** is not perceptibly sensitive to air, but should be stored under inert gas. Oxygen impurities in the reaction mixture should be avoided because they become trapped in by-products. The composition of **2** was determined by X-ray diffraction on single crystals and confirmed by energy-dispersive X-ray spectroscopy (EDX) analysis (Figure S2, Supporting Information).

2.2. Crystal Structure

A single crystal of **2** was investigated by X-ray diffraction at RT (Table S2, Supporting Information). The cell metrics suggested an *F*-centered orthorhombic lattice; accordingly, the crystal structure of **2** was initially solved and refined in the orthorhombic space group *Fmmm*. The figures of merit of the refinement as well as the resulting structure model were quite reasonable, with the exception of a 50% occupancy of the single crystallographic copper position. Therefore, refinements were performed in space groups of lower symmetry that allow the position to be split. Among the four possible ordering models tested, the monoclinic model presented here was the only one that was refined to a fully ordered distribution of the copper atoms (Table S3, Supporting Information). We used the monoclinic space group *F* 1 2/*m* 1, a nonstandard setting of *C* 1 2/*m* 1, with pseudoorthorhombic metrics ($a = 9.1697(4)$ Å, $b = 15.8050(6)$ Å, $c = 18.2437(5)$ Å, $\beta = 90.103(2)^\circ$). The proximity to the symmetry of the crystal class *mmm* causes pseudomerohedral twinning along [100]. Moreover, the unit cell has a pseudoorthohexagonal basis ($b/a - \sqrt{3} = 0.008$).

In the crystal structure of **2** (Figure 1, 3), positively charged intermetallic layers $[(\text{Bi}_4\text{Rh})_3\text{I}]^{2+}$ and layers of anionic spacers $[\text{Cu}_2\text{I}_4]^{2-}$ alternate along the [001] direction. The intermetallic layer is a kagome net of edge-sharing rhodium-centered bismuth cubes that hosts an iodide ion in each of its hexagonal-prismatic voids (Figure 3). It has the symmetry of the 2D subperiodic layer group *p* 6/*m* *m* *m* (no. 80). The spacer layer is a packing of discrete centrosymmetric tetraiodido-dicuprate(I) anions (Figure 3). The copper cations are in trigonal-planar coordination, with one terminal and two μ -bridging iodide ions each. The layer group symmetry is *c* 1 2/*m* 1 (no. 18). The projection of the stacking vector on the (001) plane, i.e., the lateral offset of neighboring layers of the same kind, is exactly $a/2$ (in **1**, this is $a/6$). The hexagonal pseudosymmetry of the intermetallic layer allows stacking vectors rotated by 120° and 240°. In the investigated crystal of **2**,

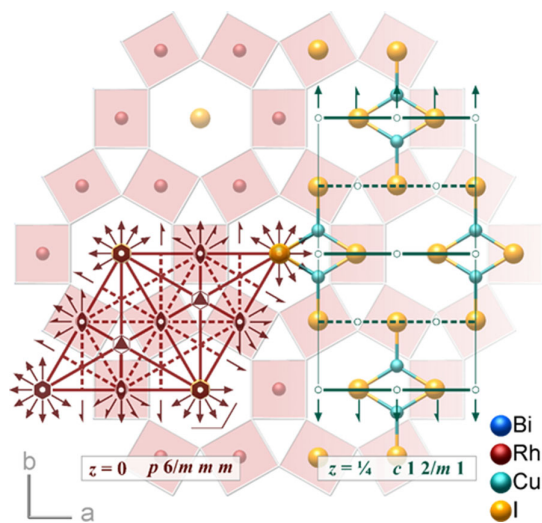


Figure 3. Intermetallic layer $[(\text{Bi}_4\text{Rh})_3\text{I}]^{2+}$ (centered at $z = 0$) and spacer layer $[\text{Cu}_2\text{I}_4]^{2-}$ (centered at $z = \frac{1}{4}$) in **2**. The symmetry diagrams of the respective layer groups are superimposed.

such stacking faults occur with about 1% probability and are responsible for the highest maxima of the residual electron density. In view of this massive pseudosymmetry, the fairly well-ordered crystal requires a mechanism to pass information about order through the structure. This is apparently achieved by the $[\text{Cu}_2\text{I}_4]^{2-}$ groups, which do not only imprint a preferred orientation in the (001) plane and thus cancel the hexagonal symmetry, but are intercalated to reach into the hexagonal voids of both neighboring intermetallic layers, thereby interlocking them.

The bond lengths Rh–Bi (2.80–2.85 Å) and Bi–Bi (3.17–3.46 Å) in **2** (Table S4, Supporting Information) deviate by less than 0.02 Å from those in **1**. Planar $[\text{Cu}_2\text{I}_4]^{2-}$ anions have been reported previously, e.g., in two modifications of $[\text{PPh}_4]_2[\text{Cu}_2\text{I}_4]$.^[25] In **2**, the Cu–I distances are 2.55 Å (terminal) and 2.61 Å (bridging), which differs by no more than 0.06 Å from that of the references. The Cu···Cu distances differ much more: 2.71 Å for **2**, while 2.85 and 2.96 Å for the phosphonium salts. However, this parameter is highly dependent on its chemical environment, e.g., for $[\text{Ba}(\text{tetraglyme})_2][\text{Cu}_2\text{I}_4]$ ^[26] it is 2.64 Å. It should also be noted that the Cu cation in **2** has two direct Bi neighbors in the distance of 3.12 Å. For comparison, 2.67 Å was reported as the average Cu–Bi distance in the $(\text{CuBi}_8)^{3+}$ cluster,^[27] and 2.74 Å as the bond length in the $[(\text{Me}_3\text{Si})_2\text{Bi}-\text{Cu}(\text{PMe}_3)_3]$ molecule.^[28]

The essential difference between the structures of **1** and **2** lies in the nature and thickness of their spacer layers. The $[\text{Cu}_2\text{I}_4]^{2-}$ groups of **2** replace the $[\text{Bi}_2\text{I}_8]^{2-}$ chains of **1** without changing the layer charge. The substitution only slightly affects the lateral layer dimensions: $[a(2)-a(1)]/\bar{a} = 4 \times 10^{-4}$, $[b(2)-b(1)]/\bar{b} = -2 \times 10^{-3}$. The spatial density of the TI channels in the stacking direction was increased to 1.1 nm^{-1} and seems to represent the maximum feasible. However, the question arises whether the spacer in **2**, which is only one atom thin, is as efficient an electronic separator as the spacer in **1**, which is three atoms thick. The subiodides $\text{Bi}_{13}\text{Pt}_3\text{I}_7$ ^[17,18] (**3**) and $\text{Bi}_{12}\text{Pt}_3\text{I}_5$ ^[18] (**4**) have basically the same intermetallic layers and contain monolayers of isolated iodide ions as spacers. **4** is even isostructural to **2**, except that it does not have copper cations within the iodide spacer layer. The distance between intermetallic TI layers is about 0.6 Å wider in the copper-containing compound **2** than in **4**, suggesting a significant difference in chemical bonding between TI and spacer layers.

2.3. Chemical Bonding

A density functional theory (DFT)-based real-space bonding analysis of **2** confirms strong covalent bonding within the two types of layers and mainly electrostatic interactions between them, similar to the parent compound **1**.^[16] In **Figure 4a**, the green isosurface of the electron density (at 0.035 a.u.) shows that the $[\text{Cu}_2\text{I}_4]^{2-}$ group (in the center) is clearly separated from the neighboring intermetallic layers. In the yellow isosurface, at the much lower value of 0.0223 a.u., the electron density of both layers merges at the bond critical point, linking Bi and Cu atoms. However, there is no indication for a constructive interaction between Bi and Cu, as will be shown below.

Figure 4b depicts the electron density contribution for all states lying between the Fermi level and 0.5 eV below. The high energy electron density contribution is formed from the orbitals of all atomic species. In case of Cu, a clearly structured 3*d* orbital contribution is evident. Despite this fact, no direct Cu–Cu bond is found. The valence electron density around the Bi atom is mainly governed by its lone pair.

The absence of Cu–Cu and Cu–Bi two-center bonding is evident in the analysis of atom-specific density contributions (Table S5, Supporting Information). Here, the electron density resulting from the square of given atomic states and their respective mixtures is integrated within the unit cell. For example, choosing the 3*d* and 4*s* states for one of the Cu atoms, the resulting electron density integrates to 10.1 electrons within the unit cell, indicating a filled 3*d* shell on Cu. In the case where the 3*d* and 4*s* states are chosen for both Cu atoms, the charge distribution integrates to 20.2 electrons. As this number is equal to the simple sum of both Cu populations, there is no additional attractive interaction between the two Cu atoms. Otherwise, the integrated populations would be higher than the sum of the Cu1 and Cu2 populations because additional terms would arise from Cu1 to Cu2 mixtures. The absence of a direct Cu–Cu bond is also shown by the chemical bonding analysis based on the ELI-D.^[29] **Figure 4c** depicts an orthoslice of ELI-D through the $[\text{Cu}_2\text{I}_4]^{2-}$ group. The penultimate shell for Cu is clearly visible and shows an almost spherical distribution. No distortion or bonding region is found between the two Cu atoms. Moreover, the localization domain between the two Cu atoms emerges from the valence

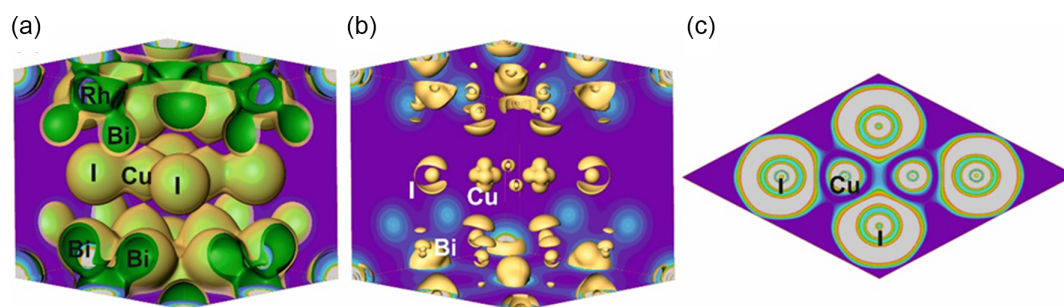


Figure 4. a) Total electron density for **2**. Isosurface at 0.035 a.u. (dark green) and at 0.023 a.u. (yellow); orthoslices depict electron density between 0 a.u. (violet) and 0.8 a.u. (white). b) Electron density contribution of states that lie between the Fermi level and 0.5 eV below. Yellow isosurface at 0.002 a.u.; orthoslices depict density contributions between 0 a.u. (violet) and 0.002 a.u. (white). The corresponding representation restricted to the highest occupied state can be found in Figure S9, Supporting Information. c) Electron-localizability indicator (ELI-D) for the $[\text{Cu}_2\text{I}_4]^{2-}$ anion in **2**. The orthoslice depicts values from 0.8 a.u. (violet) to 1.2 a.u. (white).

Table 2. Electron counts and layer distances for bismuth-rich iodides with kagome-type intermetallic nets and their observed or calculated electronic properties.

Compound	Kagome net	Spacer	Valence electrons per $[MBi_{8/2}]$ cube ^{a)}	Distance between nets [Å]	Electronic properties
Bi ₁₄ Rh ₃ I ₉ (1) ^[13]	$[(Bi_4Rh)_3]^{3+}$ I ⁻	$[Bi_2I_8]^{2-}$	$12 + 9 - 1 = 20$	9.3	Weak 3D TI gap 240 meV
Bi ₁₂ Rh ₃ Sn ₃ I ₉ ^[43]	$[(Bi_4Rh)_3]^{3+}$ I ⁻	$[Sn_3I_8]^{2-}$	$12 + 9 - 1 = 20$	9.2	Weak 3D TI gap 210 meV
Bi ₁₂ Rh ₃ Cu ₂ I ₅ (2)	$[(Bi_4Rh)_3]^{3+}$ I ⁻	$[Cu_2I_4]^{2-}$	$12 + 9 - 1 = 20$	5.9	Weak 3D TI gap 10 meV
Bi ₁₃ Pt ₃ I ₇ (3) ^[16,17]	$2 \times [(Bi_4Pt)_3]^{4+}$ $2 \times I^-$	$[Bi_2I_8]^{2-}$ $4 \times I^-$	$12 + 10 - 4/3 = 20^{2/3}$	9.3 5.3	2D semimetal pseudogap
Bi ₁₂ Pt ₃ I ₅ (4) ^[18]	$[(Bi_4Pt)_3]^{5+}$ I ⁻	$4 \times I^-$	$12 + 10 - 5/3 = 20^{1/3}$	5.3	Poor 3D metal
Bi ₃₈ Pt ₉ I ₁₄ ^[18]	$3 \times [(Bi_4Pt)_3]^{4+}$ $2 \times [BiI_2]^-$, I ⁻	$9 \times I^-$	$12 + 10 - 4/3 = 20^{2/3}$	5.6	Semiconductor vanishing gap

^{a)}Each Bi atom contributes its three *6p* electrons (the 6s electrons form lone pairs), Rh nine electrons, and Pt ten electrons; the positive charge has to be subtracted.

region of the bridging I atoms. Despite the prominent bond critical point between Bi and Cu in the electron density, there is no direct bond because the integrated electron density contribution for *3d/4s* states of both Cu atoms and *6s/6p* states of all Bi atoms yields 72.4 electrons, which is the sum of the individual Bi and Cu contributions.

In compounds **3** and **4**, which contain monolayers of iodide ions, the Bi–I–Bi bonds connecting adjacent intermetallic layers are covalent to a significant extent. In **3**, they cause pairwise coupling of the intermetallic layers, resulting in a semimetal with a pseudogap or, below 3 K, a superconductor (Table 2 and Figure S9, Supporting Information).^[18,21] In the band structure of **4** (SOC included), a band crosses the Fermi level along the stacking direction.^[18] In **2**, the Cu cations have a special role, as they redirect the covalent bonding predominantly to Cu–I and render the Bi⋯I interactions more electrostatic. Moreover, as both Bi and Cu atoms are positively charged and close to each other in stacking direction, the related repulsion together with the reduced covalent interlayer bonding leads to a large distance between TI layers which is 0.6 Å wider in the copper compound **2** than in the almost isostructural copper-free compound **4** (see Table 2). Reduced covalency and large spacing result in low electronic interaction between adjacent TI layers.

The synopsis in Table 2 suggests a fairly simple distance criterion for the occurrence of TI properties in this class of compounds. The intermetallic kagome nets should be at least 5.9 Å apart, as is the case in **2**. A thicker spacer layer also generates a wider topological gap. This effect seems to saturate at distances above 9 Å. There the topological gap is mainly determined by the band splitting due to SOC, while band dispersion by chemical bonding along the stacking direction plays only a minor role. Of course, a matching electron count is also required to prevent bulk metallic conductivity.

2.4. Electronic Band Structure and Topology

Figure 5 shows the total and layer-resolved densities of states (DOS) as well as the electronic band structure of **2**. These data were obtained within the generalized gradient approximation (GGA) with spin–orbit effects included in a nonperturbative manner using a four-component Kohn–Sham–Dirac approach implemented in the FPLO code.^[30] The ground state corresponds to a nonmagnetic semiconductor with an indirect gap of approximately 10 meV. In view of the fact that the bandgap of **2** is much smaller than the gap of **1** (240 meV), it is possible that structure optimization may lead to an enhancement of the bandgap. To this end, we computed the residual forces on each atom using the symmetry constraints for the space group. We found that the maximum force on any atom is only about 7 meV Å⁻¹. Even after relaxing the symmetry constraints (space group *P* 1 with 22 inequivalent atoms in the unit cell), the maximum force on any atom was smaller than 10 meV Å⁻¹. This test confirms the experimental structure and leaves no room for gap enhancement by structure optimization.

Calculations without SOC result in a metallic state, suggesting that the gap is SOC-induced and may have an inverted parity sequence. To ascertain the nontrivial topological properties, we computed the Z_2 invariants.^[31] We find $Z_2 = (0; 001)$, implying that **2** is a weak 3D TI predicted to possess no protected surface states in the (001) surface, but on other crystal faces.^[31] Space group symmetry contains mirror symmetry $m(\gamma)$ and, therefore, allows a topological crystalline insulator phase. However, such a phase in **2** is ruled out by explicit computation of the mirror Chern number.^[32]

In analogy to **1**,^[16] the states around the gap in the electronic band structure are dominated by the atoms of the intermetallic TI layer, especially the *6p* states of Bi (see Figure 5, S10, Supporting Information). This is, on one hand, the basis for the SOC

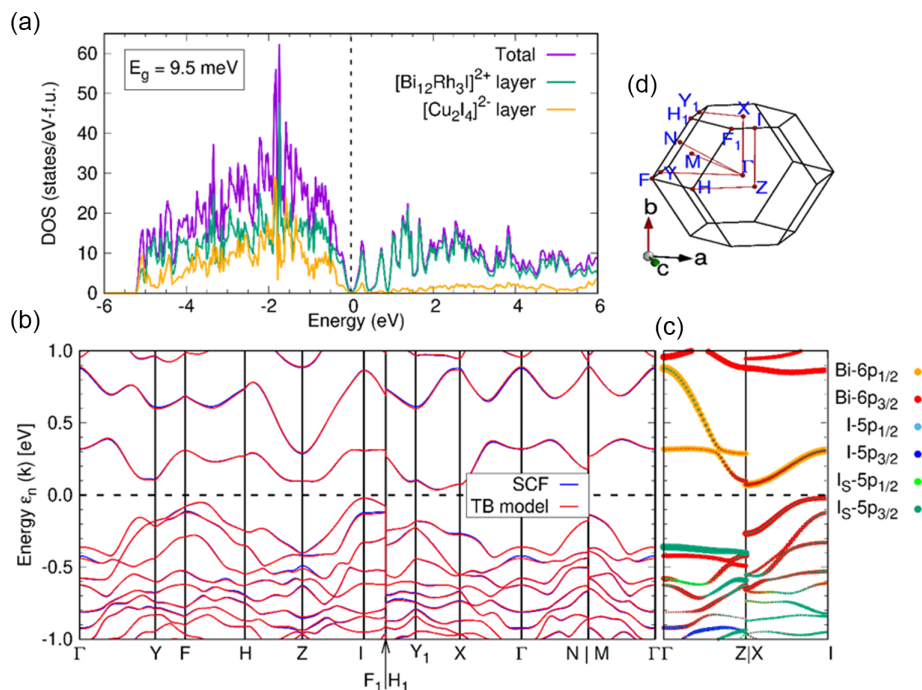


Figure 5. a) Total and layer-resolved DOS of **2** as obtained in a fully relativistic GGA calculation. b) Self-consistent (blue) band structure obtained within a fully relativistic GGA calculation and the related Wannier TB-model-derived (red) band structure of $\text{Bi}_{12}\text{Rh}_3\text{Cu}_2\text{I}_5$ (**2**). c) Layer-resolved contributions from the Bi $6p$ orbitals and I $5p$ orbitals from the intermetallic layer as well as the spacer layer (labeled I_S) along Γ -Z and X-I. d) Brillouin zone. The Fermi energy was set to $\epsilon_F = 0$ and is shown by a dashed line.

generated parity inversion and, on the other hand, the reason why an exchange of the spacer layer does not necessarily affect the 3D TI properties within this family of compounds. Specifically, DFT calculations for a charge-compensated $[(\text{Bi}_4\text{Rh})_3\text{I}]$ layer suggests that the intermetallic layer is a 2D TI.^[16a] A 2D TI is characterized by an odd number of odd parities of the filled electronic states at the four time-reversal invariant momenta (TRIM) Γ_i^{2D} ($i = 1, \dots, 4$). This holds for a system with inversion symmetry, where $\Gamma_i^{2D} = (n_1\mathbf{b}_1 + n_2\mathbf{b}_2)/2$ with $n_j = (0, 1)$ and \mathbf{b}_j denotes the reciprocal lattice vectors.^[31] If a periodic stack of 2D TI layers with appropriate spacer layers is formed, each 2D TRIM point is split into a pair of TRIM points in the 3D reciprocal space, $\Gamma_{i,n_3}^{3D} = \Gamma_i^{2D} + n_3\mathbf{b}_3/2$ with $n_3 = (0, 1)$. A sufficient condition for the formation of a weak 3D TI with $Z_2 = (0; 001)$ is that, the spacer layer preserves, up to a gauge transformation,^[31] the parity at the 2D TRIM points Γ_i^{2D} in the related 3D pair $(\Gamma_{i,0}^{3D}, \Gamma_{i,1}^{3D})$. We suggest that this preservation of parity is guaranteed if the electronic states have essentially the same orbital character all along the line between the two points Γ_{i,n_3}^{3D} . In other words, bonding among 2D TI and spacer layers should have only minor covalent contributions. Indeed, this situation is confirmed for **2**, as shown in Figure 5c: The orbital character of all bands is almost invariant in the vicinity of the Fermi level and no additional band inversions are present along the stacking direction [001].

This correlation between topological properties and chemical bonding is illustrated in the considered class of layered compounds by comparing $\text{Bi}_{12}\text{Rh}_3\text{Cu}_2\text{I}_5$ (**2**) with $\text{Bi}_{13}\text{Pt}_3\text{I}_7$ (**3**) or $\text{Bi}_{12}\text{Pt}_3\text{I}_5$ (**4**).

Earlier DFT calculations had shown that a spacer that consists of a monolayer of iodide ions leads to covalent Bi-I-Bi bonds between neighboring intermetallic layers. In **3**, covalent pairing of intermetallic layers creates a trivial topology, while in **4**, the strong inter-layer bonding leads to a metallic state even in a hypothetical strongly doped situation with even electron number.^[18,21]

2.5. Photoelectron Spectra

To gain experimental insights into the electronic properties of **2**, we carried out high-resolution angle-resolved photoelectron spectroscopy (ARPES) on two samples. Both were cleaved under UHV conditions. The photoemission experiments were carried out at a pressure of $p < 5 \times 10^{-11}$ mbar and at low temperature ($T = 20$ K). **Figure 6a** shows the normal emission spectrum of sample #1. Additional data for sample #1 and #2 are shown and discussed in the Supporting Information. While the overall agreement between the two data sets at large binding energies is very good, some differences are notable, especially near the Fermi energy. We ascribe these differences to unlike surface compositions probed in the two measurements (see Supporting Information). Most importantly, a faint dispersion-less band is observed at the Fermi energy for sample #1.

As the resolution of the measured bands was relatively low for all samples, we calculated the inverse second derivative from energy distribution curves (EDCs) as shown in **Figure 6a**, right panel, which enhances the visibility of small features in a noisy measurement. The broadening could be due to superposition of

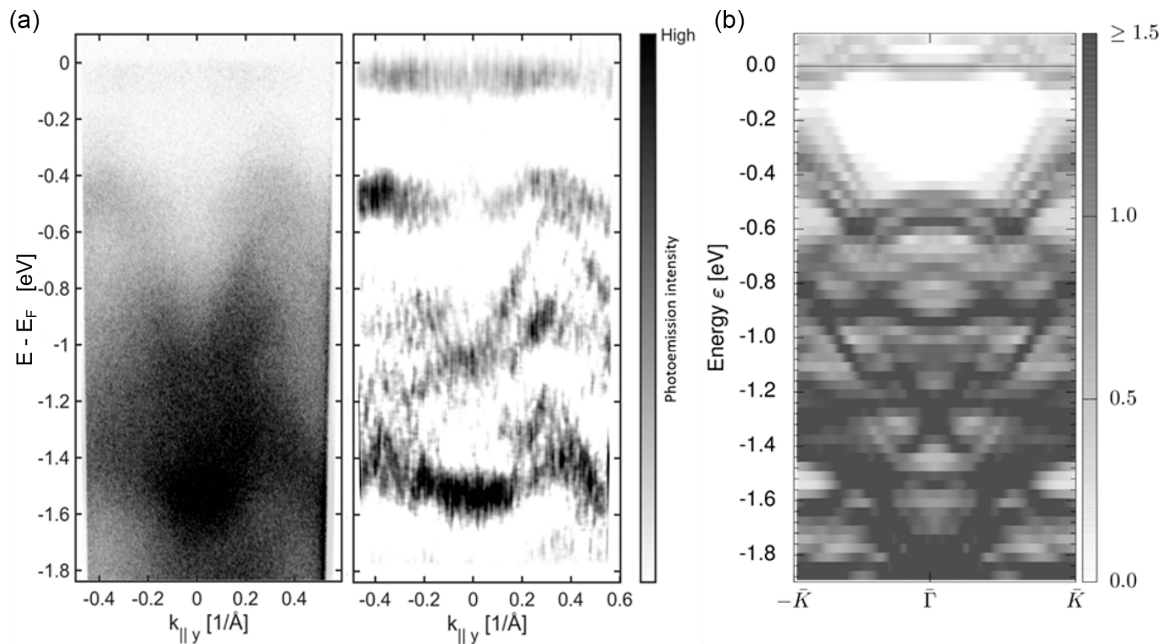


Figure 6. a) Normal emission ARPES spectrum measured at $T = 20$ K (left) and corresponding inverse second derivative plot extracted from EDCs (right). b) The simulated ARPES spectrum corresponding to a TB model for a slab of five unit cells with $[(\text{Bi}_4\text{Rh})_3\text{I}]^{2+}$ surface termination and a Gaussian broadening of 20 meV. The high symmetry points $\bar{\Gamma}$ and \bar{K} correspond to the calculated surface Brillouin zone. The distance $\bar{\Gamma}\bar{K} = 0.457 \text{ \AA}^{-1}$ (see Supporting Information for details).

signals from domains of the two possible surface terminations, as observed for **1**.^[16c]

In order to model the surface electronic properties and to understand related subtleties, we carried out tight-binding (TB) calculations for both $[(\text{Bi}_4\text{Rh})_3\text{I}]^{2+}$ and $[\text{Cu}_2\text{I}_4]^{2-}$ surface terminations in a finite-slab geometry. To this end, an accurate (bulk) TB model was obtained by considering the maximally projected Wannier functions in the energy window between -14 and $+7$ eV (see Figure 5b and Experimental Section). This TB model was then used to investigate the surface electronic properties for slabs consisting of five unit cells along $[001]$ (periodic boundary conditions along a and b). To model the ARPES spectra, layer- and k -resolved DOS were convoluted with an exponential function by considering an escape depth of 10 \AA . Further, a Gaussian broadening of 20 meV was introduced to model the experimental resolution.

In the simulated spectra, it was possible to distinguish the two different terminations of the (001) surface. The ARPES data set #1 was identified to compose dominantly of $[(\text{Bi}_4\text{Rh})_3\text{I}]^{2+}$ surface terminations. Figure 6b shows the simulated EDC for this termination. To match with ARPES data set #1, it was assumed that the Fermi energy is located about 0.10 eV above the bottom of the conduction band. This particular choice of the Fermi energy is consistent with the observed faint band at the Fermi energy. The applied shift of the Fermi level is necessary in order to model the polar surface that results in an intrinsic doping (also called band bending) that was already observed in the parent compound **1**.^[16]

While the overall qualitative agreement between the simulated and the measured ARPES spectra is evident, the quantitative agreement is also remarkably good (see Supporting Information

for a detailed quantitative comparison). In particular, the high intensities at about 0.5, 1.0, and 1.5 eV at $\bar{\Gamma}$ found in both spectra and the band dispersion (dome-shaped profile) along the $\bar{\Gamma} - \bar{K}$ path below 0.5 eV are noteworthy. The dome-shaped profile arises from the fact that the maxima of these bands do not lie at the \bar{K} point (see Figure S15, Supporting Information). This good agreement indicates that the DFT calculations of the (bulk) electronic properties correctly describe the topological properties of the real system.

Surfaces of cleaved samples have been investigated at NanoESCA beamline (Elettra, Trieste) using photoemission electron microscopy (PEEM) and micro-X-ray photoelectron spectroscopy (μ -XPS), which provide lateral resolved information about the surface. Secondary electron micrographs measured using mercury lamp, with an example shown in Figure 7a, reveal macroscopic regions that exhibit different work functions as shown in Figure 7b, where “bright” and “dark” regions are indicated. To establish the chemical composition of these regions, μ -XPS was performed revealing that the photoelectron spectra associated with the two areas differ significantly (Figure 7b,c) implying different chemical terminations. In particular, the Bi $5d$ μ -XPS spectrum acquired from the bright region shows one doublet, while from the dark region two doublets with the same width are observed. It is tempting to assign these regions to different terminations of a clean surface (bright = $[\text{Cu}_2\text{I}_4]^{2-}$; dark = $[(\text{Bi}_4\text{Rh})_3\text{I}]^{2+}$). However, the chemical shift of 2 eV in the Bi $5d$ from the dark region is much larger than expected for the $[(\text{Bi}_4\text{Rh})_3\text{I}]^{2+}$ surface based on DFT calculation for few-layer slabs models (about 0.2 eV). Moreover, the

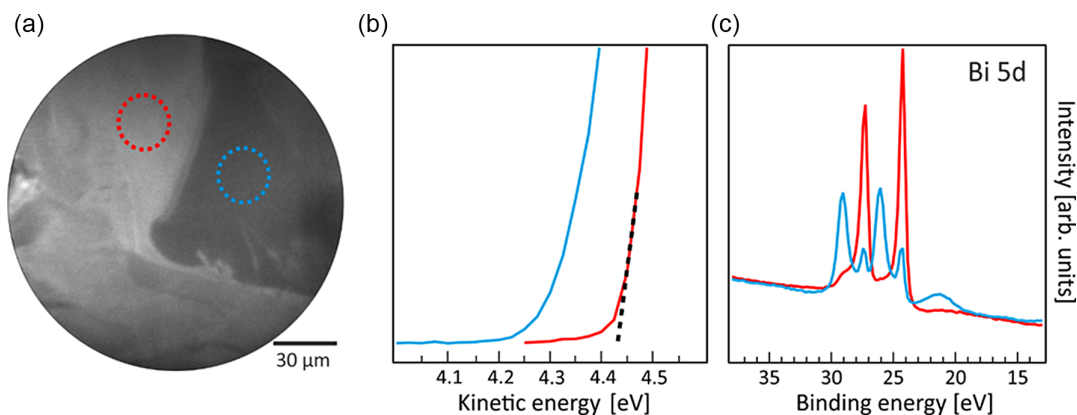


Figure 7. a) Secondary electron image acquired at a kinetic energy of 4.55 eV; red and blue circles indicate the two regions, termed “bright” (red) and “dark” (blue), from which the data were collected, with corresponding b) work function onset and c) Bi 5d μ -XPS.

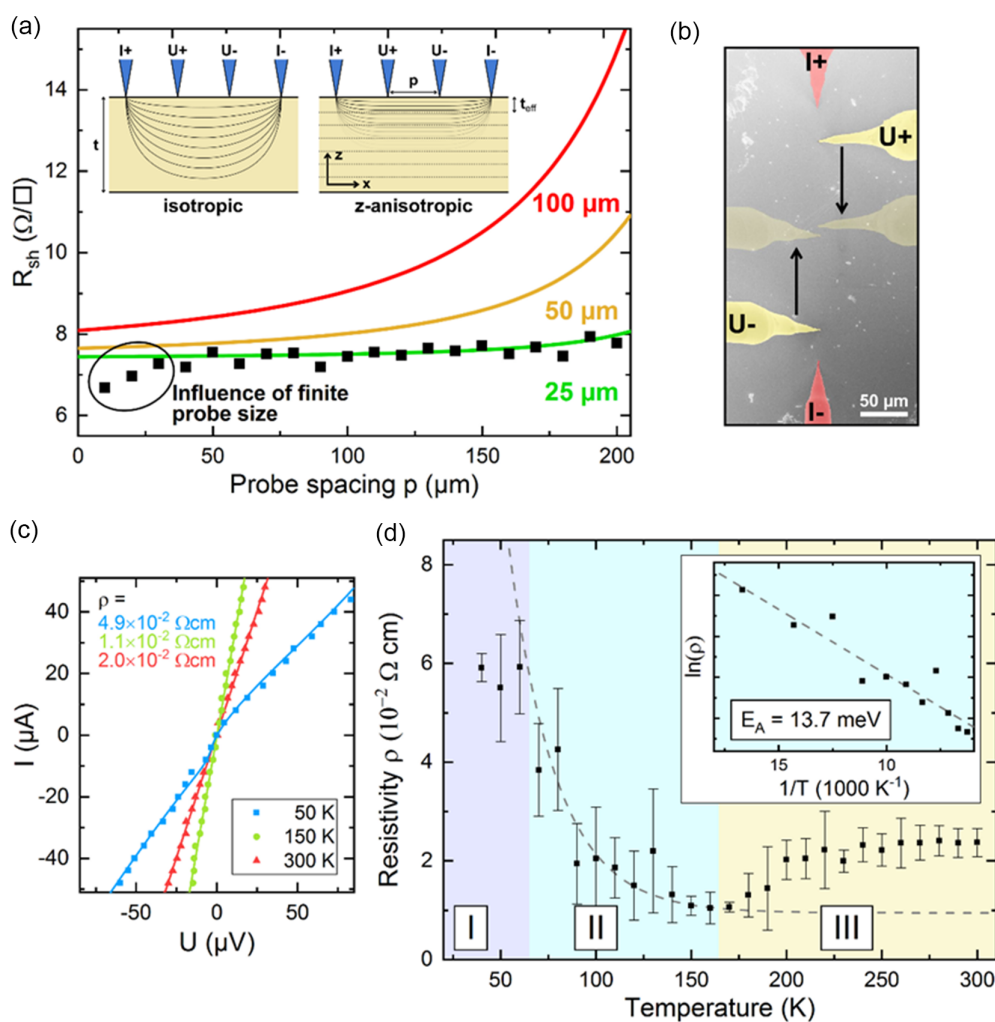


Figure 8. Resistivity of a crystal of **2** measured by in situ four-point probe technique. a) Averaged resistivity as a function of probe distance p measured at 300 K. The solid lines are simulations for various effective thicknesses t_{eff} and fixed bulk resistivity. For better visibility, the curves for 50 and 100 μm are scaled by a factor of 2 and 4, respectively. b) Scanning electron microscopy (SEM) image of the collinear four-point probe geometry. The current-probes $I_{+,-}$ remained fixed. c) $I(U)$ curves for fixed probe spacing $p = 25 \mu\text{m}$. d) Temperature-dependent resistivity (squared tip configuration, $p = 30 \mu\text{m}$). Inset: Arrhenius plot of regime II revealing an activation energy of about 14 meV.

appearance of the 21 eV peak, which is routinely assigned to O 2s, points to (at least partial) surface contamination in the “dark” regions, probably by glue residues. Therefore, μ -XPS shows that a UHV cleaving procedure yields a clean surface for significant parts of the surface consistent with high-resolution ARPES investigations.

2.6. Electronic Transport

In order to investigate the electronic properties of this new TI compound further, we performed in situ four-point probe transport measurements using W tips. The resistivity of the sample with a thickness of $t \approx 250 \mu\text{m}$ measured at 300 K is about $7 \Omega \square^{-1}$ and does not depend on the spacing p between the tips (Figure 8a,b), which indicates 2D transport parallel to (001). A detailed analysis gave an effective thickness of the surface-near 2D channel of $t_{\text{eff}} \leq 25 \mu\text{m}$. The resistivity across the layered structure is higher by a factor of about 100 ($t/t_{\text{eff}} = \sqrt{\rho_z/\rho_{x(y)}}$),^[33] quantifying the anisotropy of the structure of compound 2. The sheet resistance for the effective 2D channel refers to a bulk resistivity of around $2 \times 10^{-2} \Omega \text{cm}$ at 300 K and is comparable to carbon.

Based on the ARPES and DFT results, we propose here a simple model for the surface-near transport channel, which is the incoherent sum of conductances stemming from the n -doped intermetallic termination of the (001) surface, the highly anisotropic semiconducting bulk, and from states with topologically nontrivial character at the edges of all predicted TI layers. Temperature-dependent measurements between 30 and 300 K reveal three different regimes (Figure 8c,d). Between 300 and about 160 K (regime III), the resistivity gradually decreased with decreasing temperature, most likely because of a reduced electron–phonon scattering. The Arrhenius analysis in the “semiconducting” regime II (160 to 60 K) shows an activation energy, which nicely correlates with the bandgap of the crystal ($E_A = E_g/2 = 14 \text{ meV}$). Apparently, the dominant transport channel in regime II and III is mediated most likely by the bulk states. Thereby, the metallic channel of the intermetallic layer at the (001) surface is based on strongly localized states, represents only about 1% of t_{eff} , and is therefore not dominating the transport (Figure 8b,c). Most interestingly, the resistivity remains constant below 60 K (regime I). This suggests that a third transport channel is present and dominating the conductivity in this regime. A likely interpretation is a percolated network of TI edge states, in which transport is largely unaffected by temperature. Very similar observations had been made for $\text{Bi}_2\text{Te}_2\text{Se}$ and $\text{Bi}_{1.1}\text{Sb}_{0.9}\text{Te}_2\text{S}$ under high pressure.^[34] There the decoupling of topological surface states and bulk states at low temperatures was much more obvious because of the wider bandgaps and the topological classification as strong 3D TIs. Here, we reveal such behavior under normal pressure and for a weak 3D TI.

3. Conclusion

$\text{Bi}_{12}\text{Rh}_3\text{Cu}_2\text{I}_5$ (2) is a new weak 3D TI. It demonstrates that the iodidobismuthate(III) spacer layer of the known weak 3D TI $\text{Bi}_{14}\text{Rh}_3\text{I}_9$ (1) can be replaced without changing the electron

count of the intermetallic layer, in this case against iodidocuprate(I) groups. Despite the fact that the new spacer is only one atomic layer thick, representing the minimum achievable in such layered salts, the character of a weak 3D TI is preserved, however, at the price of a much smaller topological gap. The copper(I) cations between the iodide ions redirect the chemical bonding inside the spacer monolayer and thus act as a tool of (topological) bandgap engineering. The demonstrated chemical robustness of the intermetallic layers, combined with the finding that transition metal atoms can be incorporated into the spacer layer, opens up new options in the current quest for intrinsically magnetic TIs, which could form the material basis for a new type of quantum computer. Moreover, it is encouraging that even in a narrow-gap weak 3D TI the electronic transport at low temperatures appears to be dominated by the topologically protected edge states. Surface termination effects are responsible for a weak n -doping of the top intermetallic layer, but do not affect the bulk semiconductor property or the topologically protected edge states. The weak interlayer bonding is expected to allow easy exfoliation of 2, ideally down to the predicted 2D TI limit of one structural layer.

4. Experimental Section

Materials: The starting materials were prepared as follows: Bismuth (ChemPur, $\geq 99.9999\%$) was treated with H_2 at 220°C . Rhodium (ABCR, $\geq 99.9\%$) was treated twice with H_2 at 500°C . Copper (pieces, Merck, p.a. grade) was treated with warm glacial acetic acid for 5 min and dried in an argon gas flow. Fresh shavings of the metal were obtained by filing it off from the treated pieces. BiI_3 (Merck-Schuchardt, $\geq 99\%$) was sublimated twice. All the starting materials were stored in an argon-filled glove box ($p(\text{O}_2)/p_0 < 1 \text{ ppm}$, $p(\text{H}_2\text{O})/p_0 < 1 \text{ ppm}$) directly after their purification.

Synthesis of $\text{Bi}_{12}\text{Rh}_3\text{Cu}_2\text{I}_5$ (2): In argon atmosphere, a stoichiometric mixture of the starting materials with the molar ratio Bi:Rh:Cu:I = 12:3:2:5 was ground in an agate mortar and sealed in a silica ampoule of about 3 mL under vacuum. For obtaining a phase-pure powder (Figure S3, Supporting Information), the sample was heated from RT to 420°C at 200 K h^{-1} and annealed at that temperature for at least 4 days. The ampoule was then quenched in water at RT. Larger crystals were obtained by heating the ampoule from RT to 700°C at a rate of 350 K h^{-1} , holding the temperature for 1–2 h, then fast cooling to 493°C at -2 K min^{-1} , followed by slow cooling to 365°C at -1 K h^{-1} and annealing at this temperature for at least 3 days. Afterward, the ampoule was quenched in water at RT. This temperature program usually yielded by-products, from which the crystals of the target phase were manually selected based on their morphology.

SEM and EDX: SEM was performed using a SU8020 electron microscope from Hitachi equipped with a triple detector system for secondary low energy and back scattered electrons was used ($U_{\text{acc}} = 2 \text{ kV}$). Figure S2, Supporting information, shows the layered morphology of the crystals of $\text{Bi}_{12}\text{Rh}_3\text{Cu}_2\text{I}_5$ (2), which usually present numerous terraces perpendicular to the stacking direction of the layers. EDX data were collected using an Oxford Silicon Drift X-MaxN detector ($U_{\text{acc}} = 20 \text{ kV}$). A polycrystalline sample was selected from the same batch as the single crystal studied by X-ray diffraction. The sample was fixed on a double-side adhesive C-pad settled on an aluminum holder. The average of a five-point analysis revealed the chemical composition of $\text{Bi}_{11.9(4)}\text{Rh}_{2.9(2)}\text{Cu}_{2.3(2)}\text{I}_{4.8(2)}$ (Figure S4, Supporting Information, right).

Thermal Analysis: DSC was performed to investigate formation and decomposition processes in the quaternary Bi–Rh–Cu–I system. A Setaram Labsys ATD-DSC device with a k -probe (Ni–Cr/Ni–Al) and Al_2O_3 as reference were used. The temperature program consisted of two cycles from 20 to 800°C to 20°C (temperature ramp: $\pm 2 \text{ K min}^{-1}$). The samples were either a mixture of the starting materials (Figure 2

and Table 1) or manually picked crystals of **2** (Figure S1 and Table S1, Supporting Information). Samples containing 40–90 mg of the starting mixture were sealed in tiny silica ampoules (also used for DSC experiments) and heated at 2 K min^{-1} from RT to 265, 297, 358, 520 or $600\text{ }^{\circ}\text{C}$ (Figure S4–S8, Supporting Information). Then the samples were annealed at the respective temperature for about 1 h and subsequently quenched in water at RT.

X-Ray Diffraction: Powder X-ray diffraction experiments were performed on an X'Pert Pro Powder diffractometer (PANalytical) with Bragg–Brentano geometry, equipped with a Ge(220) hybrid monochromator and PIXcel detector, using $\text{Cu K}\alpha_1$ radiation ($\lambda = 154.056\text{ }\mu\text{m}$). Reference crystallographic information files were taken from the Inorganic Crystal Structure Database (ICSD) or SpringerMaterials (SM) and the diffraction patterns were calculated using Jana 2006.^[35] Single-crystal X-ray diffraction data were obtained using an Apex-II kappa CCD diffractometer (Bruker) with graphite-monochromated $\text{Mo K}\alpha$ radiation ($\lambda = 71.073\text{ }\mu\text{m}$) at $296(1)\text{ K}$. Numerical absorption correction was applied based on an optimized crystal shape description. The structure was solved with direct methods and subsequent refinements against F_o^2 .^[36] For experimental details and structure data, see Table S2 and S3, Supporting Information. The transformation from *oF* to the standard *mC* setting is given in the Supporting Information. Graphics of the crystal structures were developed with diamond.^[37] Further details of the crystal structure determination are available from the Fachinformationszentrum Karlsruhe, D-76 344 Eggenstein-Leopoldshafen (Germany), E-mail: crysdta@fiz-karlsruhe.de, on quoting the depository number CSD-2079929.

Band Structure Calculations: The density functional calculations for the *C2/m* representation of the experimental structure given in Table S3, Supporting Information, were carried out using the full-potential local-orbital (FPLO) code, version 18.57.^[30] For the local density approximation (LDA), the Perdew Wang parameterization^[38] was used, while for the GGA the Perdew–Burke–Ernzerhof implementation^[39] was used. Due to the large atomic mass of the involved elements, fully relativistic (four-component Dirac) self-consistent calculations were carried out for the experimental structure. Reciprocal space integrations were performed using a linear tetrahedron method on a *k*-mesh with $12 \times 12 \times 12$ intervals in the Brillouin zone. Analysis of the electronic topological properties was carried out by calculating the Z_2 invariants following the Fu–Kane prescription,^[31] based on parity eigenvalues at the TRIM, as implemented in the FPLO code.

We also computed the residual forces on each atom using the default scalar relativistic approximation implemented in FPLO and a one-step calculation for both constrained *C2/m* space group symmetries and without it (space group *P1*). For the symmetric case, we find that the maximum force on any atom is only about $7\text{ meV } \text{Å}^{-1}$. Even after relaxing the symmetry constraint, the maximum force on any atom was $\leq 10\text{ meV } \text{Å}^{-1}$. All further calculations and related analyses were carried out for the experimental structure.

TB Model and Simulated ARPES Spectra: A TB model was constructed from the DFT band structure using the PYFPLO module which generates maximally projected Wannier functions. A full-relativistic basis set with (j, m_j) states for the 6s, 6p orbitals of Bi, 5s, 5p orbitals of I, 4d, 5s orbitals of Rh, and 3d, 4s orbitals of Cu atoms (leading to a 196 dimensional vector) was used to describe the full relativistic bands in the energy window between -14 and $+7\text{ eV}$. Figure 5b shows a comparison of the resulting TB model with the self-consistent bulk DFT band structure. Except at the top edge of the chosen energy window, the typical energy difference between the two is below 40 meV. Throughout the article, the reference Fermi energy in the DFT calculations is set to $\epsilon_F = 0$.

The weak TI properties of the TB model were also confirmed by explicitly computing the Z_2 indices which were found to be identical to the DFT results. This TB model is used to obtain the surface electronic properties (simulated ARPES spectra) based on finite-slab calculations.

In order to compare with the ARPES data, it is important to consider surface effects. As the crystal structure comprises van der Waals separated layers, we consider both surface terminations, namely, the $[(\text{Bi}_4\text{Rh})_3]^{2+}$ and the $[\text{Cu}_2\text{I}_4]^{2-}$ surface. For this sake, we use slabs with both surface terminations present on either end. The band structures along the high

symmetry paths in the SBZ were then obtained for slabs of different thicknesses, where each slab configuration consists of $n - 1$ “bulk” unit cells of the *n*-cell slab and the remaining cell is split into the two different surface half cells, i.e., into the $[(\text{Bi}_4\text{Rh})_3]^{2+}$ and the $[\text{Cu}_2\text{I}_4]^{2-}$ layers. In particular, we consider the five-cell slab which captures the surface electronic properties well. The sensitivity of the surface (simulated ARPES) spectra was further checked by comparing finite slabs consisting of 5, 10, and 20 cells, which result in a quantitatively similar spectrum.

For a quantitative comparison with ARPES spectra, however, considering the contributions of surface and bulk states (as described above) with equal weights may not be appropriate. Alternatively, one should convolute the layer- and *k*-resolved DOS with an exponentially decaying function such that intensity for layers away from the surface is successively smaller. To this end, we split each unit cell into two layer types, $[(\text{Bi}_4\text{Rh})_3]^{2+}$ and $[\text{Cu}_2\text{I}_4]^{2-}$. Starting from the $[(\text{Bi}_4\text{Rh})_3]^{2+}/[\text{Cu}_2\text{I}_4]^{2-}$ surface, which has the intensity I_0 , contributions from other layers (away from the surface) is scaled by a factor of $e^{-d/\lambda}$, where d is the average distance of the block from the surface and λ is chosen to be 10 Å . In our calculations, we consider the separation between the $[\text{Cu}_2\text{I}_4]^{2-}$ and $[(\text{Bi}_4\text{Rh})_3]^{2+}$ layers to be 5 Å . The escape depth of 10 Å suggests that a five-cell slab (thickness of about 50 Å) is sufficient.

It is important to note that this method does not consider any electrostatic shift of the surface electronic structures, which can only be evaluated by charge self-consistent slab calculations. From experiments on the parent compound **1**,^[16c] it is known that, upon cleaving, iodine ions are transferred from the spacer surface to the intermetallic $[(\text{Bi}_4\text{Rh})_3]^{2+}$ surface. This transfer is expected to compensate a large part of the surface polarity.^[16d] However, intrinsic *n*-doping has been observed in ARPES,^[16e] which is a sign of incomplete compensation that has to be taken into account in our comparison between ARPES and TB. We would like to emphasize that it is unknown to what extent the surface polarity is compensated for the present compound and under the applied cleavage conditions. Thus, it makes more sense to rely on the applied TB model that assumes complete compensation and to consider the remaining real polarity by shifting the Fermi level in the comparison with ARPES, than to perform charge self-consistent DFT slab calculations with ad hoc assumptions for the real surface structure.

Bonding Analysis: Bonding analysis for **2** was performed with the program package DGrid^[40] based on the solid-state calculation obtained with the help of the FHI-aims package.^[41] Scalar relativistic density functional calculations were performed using the PBE functional^[39] and tight basis sets for all atomic species with $5 \times 5 \times 4$ *k*-points in the Brillouin zone using Stratmann integration and Gauss broadening of 0.1 eV . Evaluation of real space properties based on the ELI-D^[29] have been evaluated on a 0.05 Bohr grid mesh.

Photoelectron Spectroscopy: The samples were cleaved under UHV conditions at a residual gas pressure of $p < 10^{-9}$ mbar. High-resolution ARPES measurements were carried out at low temperature ($T = 20\text{ K}$) using a nonmonochromatized helium discharge lamp, which provided photons of $h\nu = 21.22\text{ eV}$, and an MBS A1 hemispherical energy analyzer, which was set to an energy resolution of 20 meV . In order to obtain constant energy contours, we scanned the emission angles perpendicular to the analyzer entrance slit via the deflector lens.

Microarea XPS (μ -XPS) and work function measurements were performed at the NanoESCA beamline at Elettra (Trieste, Italy).^[42] The secondary electron images were acquired in a PEEM setup, using a high-pressure mercury lamp as excitation source. The work function and μ -XPS (spot size about $20\text{ }\mu\text{m}$) data were taken at a photon energy of 50 and 160 eV using *s*-linearly polarized light. All measurements were performed while keeping the sample at 90 K with an overall energy resolution of 50 meV and spatial resolution of 100 nm .

Electronic Transport Measurements: Four-point probe transport experiments were performed under ultrahigh vacuum conditions in the temperature range between 300 and 30 K by means of a four-tip scanning tunneling microscope (STM) system (Omicron nanoprobe system) using NaOH-etched W tips with typical radii of 100 nm . Crystals (about $250\text{ }\mu\text{m}$ thickness) were mounted on a transferable sample plate. The W tips were navigated and positioned individually in the field of view of a SEM across

the sample. This allows various probe geometries and defined probe spacing. Thereafter, each of the W tips were approached into a tunneling contact and subsequently lowered by piezo actuators in the feedback-off mode in order to ensure stable ohmic contacts. The resistance values were corrected to calculate the resistivity of the sample. The resistivity was measured at various positions and probe currents (1–100 μ A) in order to average out the effect of chemical inhomogeneity. More details about surface sensitive four-point probe measurements using collinear and squared contact assemblies can be found elsewhere.^[33]

Supporting Information

Supporting Information is available from the Wiley Online Library or from the author.

Acknowledgements

The authors thank Dr. I. Kuhnert (TU Dresden) for measuring the DSC data, U. Nitzsche (IFW Dresden) for her efforts in establishing and maintaining the IFW high-performance computational environment, and Dr. A. Koitzsch (IFW Dresden) for helpful comments on the XPS data. K.F. wishes to thank Dr. M. Kohout (MPI CPFS Dresden) for fruitful discussions and substantial encouragement over years. R.R. thanks Dr. I. C. Fulga (IFW Dresden) for helpful discussions. E.C.A. is grateful for the support given by the National Agency for Research and Development (ANID) and the German Academic Exchange Service (DAAD) as part of the scholarship program: Becas Chile Conicyt-DAAD 2017–62170004. The Technische Universität Dresden is acknowledged for funding of K.F. in terms of a Maria Reiche fellowship. T.H. was partly funded by the Deutsche Forschungsgemeinschaft (DFG, German Research Foundation) under Germany's Excellence Strategy – Cluster of Excellence Matter and Light for Quantum Computing (ML4Q) EXC 2004/1 – 390534769. The authors acknowledge financial support by the Deutsche Forschungsgemeinschaft (DFG, German Research Foundation) through the Priority Program SPP 1666 (project-id PL 712/2-1) and under Germany's Excellence Strategy through the Würzburg–Dresden Cluster of Excellence on Complexity and Topology in Quantum Matter—ct.qmat (EXC 2147, project-id 390858490).

Open access funding enabled and organized by Projekt DEAL.

Conflict of Interest

The authors declare no conflict of interest.

Data Availability Statement

The data that support the findings of this study are available in the supplementary material of this article.

Keywords

crystal structures, electronic structures, electronic transport, layered compounds, spin–orbit coupling, subvalent compounds, topological insulators

Received: August 30, 2021

Revised: November 11, 2021

Published online: January 22, 2022

- [1] a) M. Z. Hasan, C. L. Kane, *Rev. Mod. Phys.* **2010**, *82*, 3045; b) X.-L. Qi, S.-C. Zhang, *Phys. Today* **2010**, *63*, 33; c) J. Wang, S.-C. Zhang, *Nat. Mater.* **2017**, *16*, 1062.
- [2] S. S. Hong, Y. Zhang, J. J. Cha, X.-L. Qi, Y. Cui, *Nano Lett.* **2014**, *14*, 2815.
- [3] A. Asgharpour, C. Gorini, S. Essert, K. Richter, I. Adagideli, *Phys. Rev. B* **2020**, *102*, 035401.
- [4] J. Moore, *Nature* **2010**, *464*, 194.
- [5] J. Alicea, *Rep. Prog. Phys.* **2012**, *75*, 076501.
- [6] C. L. Kane, E. J. Mele, *Phys. Rev. Lett.* **2005**, *95*, 146802.
- [7] M. König, S. Wiedmann, C. Brüne, A. Roth, H. Buhmann, L. W. Molenkamp, X.-L. Qi, S.-C. Zhang, *Science* **2007**, *318*, 766.
- [8] a) A. Isaeva, M. Ruck, *Inorg. Chem.* **2020**, *59*, 3437; b) N. Kumar, S. N. Guin, K. Manna, C. Shekhar, C. Felser, *Chem. Rev.* **2021**, *121*, 2780.
- [9] a) H. Zhang, C.-X. Liu, X.-L. Qi, X. Dai, Z. Fang, S.-C. Zhang, *Nat. Phys.* **2009**, *5*, 438; Y. L. Chen, J. G. Analytis, J.-H. Chu, Z. K. Liu, S.-K. Mo, X. L. Qi, H. J. Zhang, D. H. Lu, X. Dai, Z. Fang, S. C. Zhang, I. R. Fisher, Z. Hussain, Z.-X. Shen, *Science* **2009**, *325*, 178.
- [10] L. Barreto, L. Kühnemund, F. Edler, C. Tegenkamp, J. Mi, M. Bremholm, B. Brummerstedt Iversen, C. Frydendahl, M. Bianchi, P. Hofmann, *Nano Lett.* **2014**, *14*, 3755.
- [11] A. Zeugner, J. Teichert, M. Kaiser, T. V. Menshchikova, I. P. Rusinov, A. V. Markelov, E. V. Chulkov, T. Doert, M. Ruck, A. Isaeva, *Chem. Mater.* **2018**, *30*, 5272.
- [12] a) S. V. Savilov, V. N. Khrustalev, A. N. Kuznetsov, B. A. Popovkin, Yu. M. Antipin, *Russ. Chem. Bull.* **2005**, *54*, 87; b) P. Tang, B. Yan, W. Cao, S.-C. Wu, C. Felser, W. Duan, *Phys. Rev. B* **2014**, *89*, 041409; c) I. P. Rusinov, T. V. Menshchikova, A. Isaeva, S. V. Eremeev, Yu. M. Koroteev, M. G. Vergniory, P. M. Echenique, E. V. Chulkov, *Sci. Rep.* **2016**, *6*, 20734; d) N. Avraham, A. K. Nayak, A. Steinbok, A. Norris, H. Fu, Y. Sun, Y. Qi, L. Pan, A. Isaeva, A. Zeugner, C. Felser, B. Yan, H. Beidenkopf, *Nat. Mater.* **2020**, *19*, 610; e) G. Pacchioni, *Nat. Rev. Mater.* **2020**, *5*, 332; f) A. Zeugner, M. Kaiser, P. Schmidt, T. Menshchikova, I. Rusinov, A. Markelov, W. Van den Broek, E. V. Chulkov, T. Doert, M. Ruck, A. Isaeva, *Chem. Mater.* **2017**, *29*, 1321; g) M. Lê Anh, P. Potapov, A. Lubk, T. Doert, M. Ruck, *npj 2D Mater. Appl.* **2021**, *5*, 22.
- [13] a) R. C. Vidal, A. Zeugner, J. I. Facio, R. Ray, M. H. Haghghi, A. U. B. Wolter, L. T. Corredor Bohorquez, F. Caglieris, S. Moser, T. Figgemeier, T. R. F. Peixoto, H. B. Vasili, M. Valdivares, S. Jung, C. Cacho, A. Alfonsov, K. Mehawat, V. Kataev, C. Hess, M. Richter, B. Büchner, J. van den Brink, M. Ruck, F. Reinert, H. Bentmann, A. Isaeva, *Phys. Rev. X* **2019**, *9*, 041065; b) A. Zeugner, F. Nietschke, A. U. B. Wolter-Giraud, S. Gaß, R. C. Vidal, T. R. F. Peixoto, D. Pohl, C. Damm, R. Hentrich, S. K. Moser, C. Fornari, C. Hee Min, S. Schatz, K. Treiber, M. Ünzelmann, M. Kaiser, F. Scaravaggi, B. Rellinghaus, K. Nielsch, C. Heß, B. Büchner, F. Reinert, H. Bentmann, O. Oeckler, M. Ruck, A. Isaeva, *Chem. Mater.* **2019**, *31*, 2795; c) M. M. Otrokov, I. I. Klimovskikh, H. Bentmann, D. Estyunin, A. Zeugner, Z. S. Aliev, S. Gaß, A. U. B. Wolter, A. V. Koroleva, A. M. Shikin, M. Blanco-Rey, M. Hoffmann, I. Rusinov, A. Y. Vyazovskaya, S. V. Eremeev, Y. M. Koroteev, V. Kuznetsov, F. Freyse, J. Sanchez-Barriga, I. R. Amiraslanov, M. B. Babanly, N. T. Mamedov, N. A. Abdullayev, V. N. Zverev, A. Alfonsov, V. Kataev, B. Büchner, B. Schwiier, S. Kumar, A. Kimura, et al., *Nature* **2019**, *576*, 416.
- [14] R. C. Vidal, A. Zeugner, J. I. Facio, R. Ray, M. H. Haghghi, A. U. B. Wolter, L. T. C. Bohorquez, F. Caglieris, S. Moser, T. Figgemeier, T. R. F. Peixoto, H. B. Vasili, M. Valdivares,

- S. Jung, C. Cacho, A. Alfonsov, K. Mehlawat, V. Kataev, C. Hess, M. Richter, B. Büchner, J. van den Brink, M. Ruck, F. Reinert, H. Bentmann, A. Isaeva, *Phys. Rev. X* **2019**, 9, 041065.
- [15] L. Fu, C. L. Kane, E. J. Mele, *Phys. Rev. Lett.* **2007**, 98, 106803.
- [16] a) B. Rasche, A. Isaeva, M. Ruck, M. Richter, K. Koepernik, J. van den Brink, *Sci. Rep.* **2016**, 6, 20645; b) B. Rasche, A. Isaeva, A. Gerisch, M. Kaiser, W. Van den Broek, C. T. Koch, U. Kaiser, M. Ruck, *Chem. Mater.* **2013**, 25, 2359; c) C. Pauly, B. Rasche, K. Koepernik, M. Liebmann, M. Pratzner, M. Richter, J. Kellner, M. Eschbach, B. Kaufmann, L. Plucinski, C. M. Schneider, M. Ruck, J. van den Brink, M. Morgenstern, *Nat. Phys.* **2015**, 11, 338; d) C. Pauly, B. Rasche, K. Koepernik, M. Richter, S. Borisenko, M. Liebmann, M. Ruck, J. van den Brink, M. Morgenstern, *ACS Nano* **2016**, 10, 3995; e) B. Rasche, A. Isaeva, M. Ruck, S. Borisenko, V. Zabolotnyy, B. Büchner, K. Koepernik, C. Ortix, M. Richter, J. van den Brink, *Nat. Mater.* **2013**, 12, 422; f) M. Lê Anh, P. Potapov, D. Wolf, A. Lubk, B. Glatz, A. Fery, T. Doert, M. Ruck, *Chem. Eur. J.* **2021**, 27, 794.
- [17] M. Ruck, *Z. Anorg. Allg. Chem.* **1997**, 623, 1535.
- [18] M. Kaiser, B. Rasche, A. Isaeva, M. Ruck, *Chem. Eur. J.* **2014**, 20, 17152.
- [19] B. Rasche, W. Van den Broek, M. Ruck, *Chem. Mater.* **2016**, 28, 665.
- [20] B. Rasche, W. Schnelle, M. Ruck, *Z. Anorg. Allg. Chem.* **2015**, 641, 1444.
- [21] B. Rasche, *Doctoral Thesis*, Technische Universität Dresden, Germany, **2016**.
- [22] a) A. Weiz, M. Lê Anh, M. Kaiser, B. Rasche, T. Herrmannsdörfer, T. Doert, M. Ruck, *Eur. J. Inorg. Chem.* **2017**, 5609; b) H. Okamoto, *Binary Alloy Phase Diagrams*, 2nd edition (Ed: T. B. Massalski), ASM International, Materials Park, OH **1990**, pp. 744–748 (as cited in “Bi-I Binary Phase Diagram 0-100 at.% I”, SpringerMaterials, online database, https://materials.springer.com/isp/phase-diagram/docs/c_0900442 (accessed: July 2021)).
- [23] H. J. Okamoto, *J. Phase Equilib. Diffus.* **2010**, 31, 204.
- [24] A. Gerisch, *Doctoral Thesis*, Technische Universität Dresden, Germany **2014**.
- [25] a) H. Hartl, I. Brüdgam, F. Mahdjour-Hassan-Abadi, *Z. Naturforsch.* **1985**, 40b, 1032; b) A. Pfitzner, D. Schmitz, *Z. Anorg. Allg. Chem.* **1997**, 623, 1555.
- [26] S. Mishra, E. Jeanneau, G. Ledoux, S. Daniele, *Inorg. Chem.* **2014**, 53, 11721.
- [27] M. Knies, M. Kaiser, A. Isaeva, U. Müller, T. Doert, M. Ruck, *Chem. Eur. J.* **2018**, 24, 127.
- [28] D. Fenske, A. Rothenberger, S. Wieber, *Z. Anorg. Allg. Chem.* **2003**, 629, 929.
- [29] a) M. Kohout, *Int. J. Quantum Chem.* **2004**, 97, 651; b) M. Kohout, K. Pernal, F. R. Wagner, Y. Grin, *Theor. Chem. Acc.* **2004**, 112, 453; c) M. Kohout, *Faraday Discuss.* **2007**, 135, 43.
- [30] a) K. Koepernik, H. Eschrig, *Phys. Rev. B* **1999**, 59, 1743–1757; b) <https://www.fplo.de> (accessed: January 2022).
- [31] L. Fu, C. L. Kane, *Phys. Rev. B* **2007**, 76, 045302.
- [32] J. I. Facio, S. K. Das, Y. Zhang, K. Koepernik, J. van den Brink, I. C. Fulga, *Phys. Rev. Mater.* **2019**, 3, 074202.
- [33] I. Miccoli, F. Edler, H. Pfnür, C. Tegenkamp, *J. Phys.: Condens. Matter* **2015**, 27, 223301.
- [34] S. Cai, J. Guo, V. A. Sidorov, Y. Zhou, H. Wang, G. Lin, X. Li, Y. Li, K. Yang, A. Li, Q. Wu, J. Hu, S. K. Kushwaha, R. J. Cava, L. Sun, *npj Quantum Mater.* **2018**, 3, 62.
- [35] V. Petricek, M. Dusek, L. Palatinus, *Z. Kristallogr.* **2014**, 229, 345.
- [36] a) G. M. Sheldrick, *SHELXL, Program for Crystal Structure Refinement—Multi-CPU*, Georg-August-Universität Göttingen, Göttingen, Germany, **2014**; b) G. M. Sheldrick, *Acta Crystallogr., Sect. A* **2008**, 64, 112.
- [37] K. Brandenburg, *Diamond 3.2k, Crystal and Molecular Structure Visualization*, Crystal Impact GbR, Bonn, Germany **2014**.
- [38] J. P. Perdew, Y. Wang, *Phys. Rev. B* **1992**, 45, 13244.
- [39] J. P. Perdew, K. Burke, M. Ernzerhof, *Phys. Rev. Lett.* **1996**, 77, 3865.
- [40] M. Kohout, *DGrid, Version 5.0*, Dresden, Germany **2016**.
- [41] V. Blum, R. Gehrke, F. Hanke, P. Havu, V. Havu, X. Ren, K. Reuter, M. Scheffler, *Comput. Phys. Commun.* **2009**, 180, 2175.
- [42] C. M. Schneider, C. Wiemann, M. Patt, V. Feyer, L. Plucinsk, I. P. Krug, M. Escher, N. Weber, M. Merkel, O. Renault, N. Barrett, *J. Electron. Spectrosc. Relat. Phenom.* **2012**, 185, 330.
- [43] M. Lê Anh, M. Kaiser, M. P. Ghimire, M. Richter, K. Koepernik, M. Gruschwitz, C. Tegenkamp, T. Doert, M. Ruck, *Chem. Eur. J.* **2020**, 26, 15549.